Chemical Engineering Journal 394 (2020) 124866

Contents lists available at ScienceDirect

Chemical Engineering Journal

journal homepage: www.elsevier.com/locate/cej

Construction of MoS_2 nano-heterojunction via ZnS doping for enhancing in-situ photocatalytic reduction of gold thiosulfate complex

Weiquan Zhan[a], Yuan Yuan[a], Bingqiao Yang[b], Feifei Jia[a,c,*], Shaoxian Song[a,c]

[a] Hubei Key Laboratory of Mineral Resources Processing and Environment, Wuhan University of Technology, Luoshi Road 122, Wuhan, Hubei 430070, China
[b] School of Xingfa Mining Engineering, Wuhan Institute of Technology, Xiongchu Avenue 693, Wuhan, Hubei 430073, China
[c] School of Resources and Environmental Engineering, Wuhan University of Technology, Luoshi Road 122, Wuhan, Hubei, 430070, China

HIGHLIGHTS

- MoS_2/ZnS nano-heterojunction is firstly proposed as a catalyst for the recovery of $[Au(S_2O_3)_2]^{3-}$ from leaching solution.
- $[Au(S_2O_3)_2]^{3-}$ can be in-situ reduced into Au^0 and efficiently recovered by MoS_2/ZnS nano-heterojunction.
- The steps of $[Au(S_2O_3)_2]^{3-}$ recovery was simplified by using MoS_2/ZnS nano-heterojunction.
- A complete Au^0 desorption from MoS_2/ZnS nano-heterojunction can be quickly achieved.

GRAPHICAL ABSTRACT

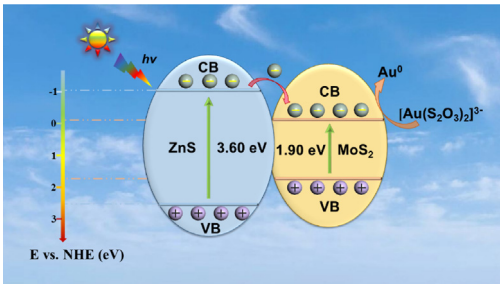

ARTICLE INFO

Keywords:
In-situ reduction
MoS_2
Nano-heterojunction
Gold thiosulfate leaching

ABSTRACT

Recovery of gold thiosulfate complex ($[Au(S_2O_3)_2]^{3-}$) from leaching solutions has been recognized as a tough task, which limited the industrial promotion of eco-friendly thiosulfate leaching technique. In this work, MoS_2/ZnS nano-heterojunction as a catalyst was proposed for the recovery of $[Au(S_2O_3)_2]^{3-}$ from leaching solution. The results indicated that $[Au(S_2O_3)_2]^{3-}$ could not only be efficiently recovered, but also in-situ reduced into Au^0 when MoS_2/ZnS nano-heterojunction being used in the leaching solution. $Mo_{0.45}Zn_{0.10}S$ exhibited an extremely high reduction capacity (1120.56 mg/g), which was 4.52 and 1.72 times of ZnS and MoS_2, respectively. The great improvement was resulted from the ZnS doping on MoS_2, which brought stronger light absorption, higher transferred efficiency and lower recombination of photogenerated electron-hole pairs of MoS_2. In addition, the Au^0 could completely desorpt from MoS_2/ZnS nano-heterojunctions in Na_2S solution in less than 4 min, leading MoS_2/ZnS nano-heterojunction to have remarkable cycling performances. This work provided a new insight for enhancing the recovery and in-situ reduction of gold thiosulfate complex from leaching solutions.

1. Introduction

Over the past decades, gold was difficultly enriched from nature ores due to its extremely low grade [1–3]. Up to date, the effective method of extracting gold from ores was leaching by cyanide [4]. However, the cyanidation leaching would cause lots of environmental problems because of the high toxicity of cyanide [5]. Under the advocating of green development in the whole world, ammoniacal thiosulfate leaching caused wide attentions owing to its relatively cheap and nontoxic process [6,7]. Thiosulfate leaching possessed not only

* Corresponding author at: Hubei Key Laboratory of Mineral Resources Processing and Environment, Wuhan University of Technology, Luoshi Road 122, Wuhan, Hubei 430070, China.
E-mail address: feifeijia@whut.edu.cn (F. Jia).

https://doi.org/10.1016/j.cej.2020.124866
Received 27 November 2019; Received in revised form 5 March 2020; Accepted 21 March 2020
Available online 23 March 2020
1385-8947/

much less environmental influences and waste treatment costs, but also technical advantages [8]. The mechanism of the application of thiosulfate leaching for extracting gold from ores could be proposed as following equation:

$$Au + 5S_2O_3^{2-} + Cu(NH_3)_4^{2+} \rightarrow Au(S_2O_3)_2^{3-} + 4NH_3 + Cu(S_2O_3)_3^{5-} \quad (1)$$

$$4Cu(S_2O_3)_3^{5-} + 16NH_3 + O_2 + 2H_2O \rightarrow 4Cu(NH_3)_4^{2+} + 12S_2O_3^{2-} + 4OH^- \quad (2)$$

Nevertheless, thiosulfate leaching technique was very difficult to be used in the industry owing to the difficulty in efficiently recovering gold from the leaching solutions.

So far, various techniques had been explored for recovering $[Au(S_2O_3)_2]^{3-}$ from leaching solutions. Cementation with zinc resulted in high reagent consumption and co-precipitation of other metals [9]. Metal displacement using copper powers was effective but not economical feasible [10]. Ion-exchange resin was applied to adsorb $[Au(S_2O_3)_2]^{3-}$, but easy pulverization of the resin and hard stripping of $[Au(S_2O_3)_2]^{3-}$ restricted the application [11]. More investigations had been focused on adsorption of $[Au(S_2O_3)_2]^{3-}$ because of its simplicity, regeneration capacity and cost efficiency [12]. However, conventional adsorbents such as active carbon [13], modified active carbon [14] and thiol- and amine-functionalized mesoporous silica [6] exhibited poor capacity in adsorbing $[Au(S_2O_3)_2]^{3-}$. In addition, conventional reductive reagents such as ascorbic acid, sodium borohydride, etc. were hardly applied in extracting $[Au(S_2O_3)_2]^{3-}$ owing to strong reducing property of reductive reagent. Kinds of ions would be reduced, resulting the difficult separation of complex solid phase. Meanwhile, the present gold recovery methods were complicated owing to the three steps including adsorption, desorption and reduction.

Considering that the reduction potential of $[Au(S_2O_3)_2]^{3-}$ to Au^0 was 0.15 eV [8], the conduction band of MoS_2 was around 0 eV [15], which was more negative than the reduction potential of $[Au(S_2O_3)_2]^{3-}/Au^0$, indicating the great possibility of the reduction of $[Au(S_2O_3)_2]^{3-}$ into Au^0. Meanwhile, according to the strong soft–soft interaction between precious metal and sulfur atoms [16,17], rich sulfur-containing MoS_2 might be very beneficial for adsorption of $[Au(S_2O_3)_2]^{3-}$ and Au^0. Based on the above considerations, it might be assumed that the adsorption, desorption and reduction processes of gold recovery from leaching solution could be accomplished by one-step procedure using MoS_2. Nevertheless, the tiny difference between the conduction band value and the reduction potential of $[Au(S_2O_3)_2]^{3-}/Au^0$ might bring poor reduction performances.

In order to enhance the ability of reducing $[Au(S_2O_3)_2]^{3-}$ into Au^0 by MoS_2, construction of heterogeneous junction on MoS_2 was a good method. Coupling another semiconductor with MoS_2 to form a straddling type band configuration was an effective approach to separate and transfer the photon-generated electrons and holes for enhancing photocatalytic activities [18–22]. Among the various semiconductors, metal sulfides was a suitable candidate for coupling with MoS_2 because of the advantage of sulfide's electronic and catalytic properties [23,24]. ZnS had wide applications in various fields, such as sensors [25–27], photovoltaic cells [28,29], biodevices [30,31] and photocatalysts [32–35] due to more negative potentials of its excited electrons, the swift generation of electron-hole pairs upon photo-excitation, biocompatibility. Simultaneously, the lattice parameters of ZnS and MoS_2 were well matched because of the formation of intimate interfaces.

To our knowledge, most materials concentrated on the adsorption not reduction of gold in aqueous solutions. It was firstly proposed for reducing $[Au(S_2O_3)_2]^{3-}$ by nano-heterojunction used in extracting gold. Thus, MoS_2/ZnS nano-heterojunction was designed for high efficiency and rapid recovery of gold from thiosulfate leaching solution in this study. The adsorption, desorption and reduction processes were accomplished by one-step using MoS_2/ZnS nano-heterojunction. MoS_2/ZnS nano-heterojunction was synthesized through a simple hydrothermal route. The in-situ reduction behaviors of $[Au(S_2O_3)_2]^{3-}$ on MoS_2/ZnS nano-heterojunction were studied in aqueous solutions. The desorption and cycling performances of MoS_2/ZnS nano-heterojunction were also researched. The objective was to make a clear understanding on the in-situ reduction behaviors of $[Au(S_2O_3)_2]^{3-}$ on MoS_2/ZnS nano-heterojunction, further to put a new way for extracting gold in leaching process.

2. Experimental

2.1. Materials

Ammonium thiosulfate ($H_8N_2O_3S_2$, 99%) was purchased from Aladdin Co. (Shanghai, China). Standard stock solutions (1000 mg/L) of chloroauric acid ($HAuCl_4$) of analytical grade was obtained from Well Group Scientific (USA) Ltd. Other reagents used in the experiment were all of analytical grade purchased from Sinopharm Chemical Reagent Co., Lsd (China). Milli-Q deionized water with a resistivity of 18.2 MΩ·cm (produced by Millipore Super Q system) was used in all the experiments.

2.2. Synthesis of MoS_2, ZnS and MoS_2/ZnS nano-heterojunction

MoS_2/ZnS nano-heterojunction was synthesized via a hydrothermal route. 2 mmol ammonium molybdate tetrahydrate ($(NH_4)_6Mo_7O_{24}{\cdot}4H_2O$), 60 mmol thiourea ($CN_2H_4S$) and various dosages of zinc chloride ($ZnCl_2$) were dissolved in 72 mL distilled water under vigorous stirring for 30 min. Then, the solution was transferred into a 100 mL Teflon-lined stainless-steel autoclave at 220 °C for 24 h. After cooling down to room temperature, the products were filtrated and washed with water for several times, followed by drying under 60 °C in vacuum. In the work, a series of MoS_2/ZnS nano-heterojunction samples with 0.2, 0.4, 0.6 and 0.8 g dosages of $ZnCl_2$ were prepared. According to the chemical component analysis, the prepared MoS_2/ZnS nano-heterojunction samples were named as $Mo_{0.49}Zn_{0.02}S$, $Mo_{0.47}Zn_{0.06}S$, $Mo_{0.45}Zn_{0.10}S$ and $Mo_{0.43}Zn_{0.14}S$, respectively. For comparison, MoS_2 and ZnS were prepared by the same procedure as mentioned above without the addition of $ZnCl_2$ or $(NH_4)_6Mo_7O_{24}{\cdot}4H_2O$.

2.3. $[Au(S_2O_3)_2]^{3-}$ reduction experimental

$[Au(S_2O_3)_2]^{3-}$ complex solution was prepared through dropwise adding $HAuCl_4$ into $H_8N_2O_3S_2$ solution under pH of 10 with the 4:1 mol ratio. Reduction experiments were conducted to study the reduction behaviors of $[Au(S_2O_3)_2]^{3-}$ on the prepared samples. Firstly, 10 mg sample was added into 150 mL 100 mg/L $[Au(S_2O_3)_2]^{3-}$ solution with pH of 10. Then the suspension was stirred with the rate of 500 rpm at room temperature under natural light with the intensity of 0.432 kW/m^2. At different time intervals (0–1440 min), 1 mL suspension was extracted and filtered with 0.22 μm filter membrane, followed by the determination of Au(I) concentration. As for studying the effect of pH on reduction, 10 mg reductants were added into 150 mL 100 mg/L $[Au(S_2O_3)_2]^{3-}$ solution with pH ranging from 8 to 12. To study the effect of $[Au(S_2O_3)_2]^{3-}$ concentration (50–150 mg/L) on the reduction, 10 mg reductants were added into 150 mL $[Au(S_2O_3)_2]^{3-}$ solution with pH of 10.

Au(I) reduction capacity was calculated by the following equation:

$$q = \frac{V_0C_0 - CV}{m} \quad (3)$$

where q meant the reduction capacity of the reductant, mg/g; C_0 and C exhibited the Au(I) concentration in the solution before and after reduction, respectively, mg/L; V_0 and V were the solution volume of the $[Au(S_2O_3)_2]^{3-}$ solution before and after reduction, respectively, L; m represented the mass of the reductant in the test, g.

2.4. Desorption of Au^0 from MoS_2/ZnS nano-heterojunction

After reaction in $[Au(S_2O_3)_2]^{3-}$ solution, MoS_2/ZnS nano-heterojunction was separated from solution through filtering. Then MoS_2/ZnS nano-heterojunction was transferred into 50 mL 0.3 mol/L Na_2S solution, and stirred at 200 rpm for 5 min. Finally, the solution was withdrawn for the determination of Au element.

Desorption efficiency of Au^0 from MoS_2/ZnS nano-heterojunctions was calculated as below:

$$R = \frac{V_1 C_1}{m_1} \times 100\% \quad (4)$$

where R represented the desorption efficiency of Au^0 from MoS_2/ZnS nano-heterojunction; V_1 meant the volume of Na_2S solution, L; C_1 was Au(I) concentration, mg/L; m_1 exhibited the mass of MoS_2/ZnS nano-heterojunction in the desorption test, mg.

2.5. Characterizations

XRD patterns were acquired on a D8 Advance system (Bruker AXS, Germany). SEM images were recorded with a Zeiss Gemini 300 (Germany). XPS was performed on an ESCALB 250Xi photoelectron spectrometer (American) with Al Kα source (1486.6 eV) for detecting the chemical state of sample. A contrAA700 continuum source atomic adsorption spectrometry system was applied to detect the concentration of Au(I). The high-resolution TEM (HRTEM) and the corresponding energy dispersive spectra (EDS) were performed on a Titan G 260–300 transmission electron microscope. Chemical component analysis of MoS_2/ZnS was measured by inductively coupled plasma optical emission spectrometer (ICP-OES, Agilent 720ES). UV–vis was recorded on a Lambda 750 S UV–vis spectrophotometer (America) using $BaSO_4$ as reference.

2.6. Electrochemical measurements

Electrochemical characterizations were conducted in three electrode cell system by a CHI1030B electrochemical station. The ITO glass deposited with reductants, Pt flake and saturated calomel electrode were used as working electrodes, counter electrode and reference electrode, respectively. 10 mg of sample was dispersed in 1 mL of ethanol containing 0.5% of nafion under ultrasound for 1 h. Next, 10 μL of the reductants dispersion was loaded onto a ITO glass serving as the working electrode. Photocurrent measurements (i-t curves) were carried out with xenon lamp with light intensity of 300 W. Na_2SO_4 (0.5 M) was applied as the electrolyte. The interval of light on/off was 30 s. Electrochemical impedance spectroscopy (EIS) was measured in a 1 M potassium ferricyanide solution over the frequency range of 0.01–10^5 Hz with an alternating current voltage of 10 mV.

3. Results and discussion

3.1. Characterization of MoS_2/ZnS nano-heterojunction

The XRD patterns of ZnS, MoS_2 and a series of MoS_2/ZnS nano-heterojunction were exhibited in Fig. 1. The diffraction peaks observed at 14.1° (0 0 2), 33.3° (1 0 0), 39.4° (1 0 3) and 59.0° (1 1 0) could be well assigned to the 2H phase MoS_2[36,37]. Meanwhile, the three pronounced peaks at 28.6° (1 1 1), 47.6° (2 2 0) and 56.6° (3 1 1) were contributed to cubic phase ZnS [38]. All the peaks of ZnS and MoS_2 were detected in MoS_2/ZnS nano-heterojunction, suggesting that little effect occurred on the crystal structure of MoS_2 and ZnS in coupling each other. Moreover, the peak intensities of MoS_2/ZnS nano-heterojunction varied with the component ratio.

The optical properties of ZnS, MoS_2 and MoS_2/ZnS nano-heterojunction were explored by UV–vis measurements, as showed in Fig. 2. Two distinct absorption shoulders from 200 to 500 nm were observed in

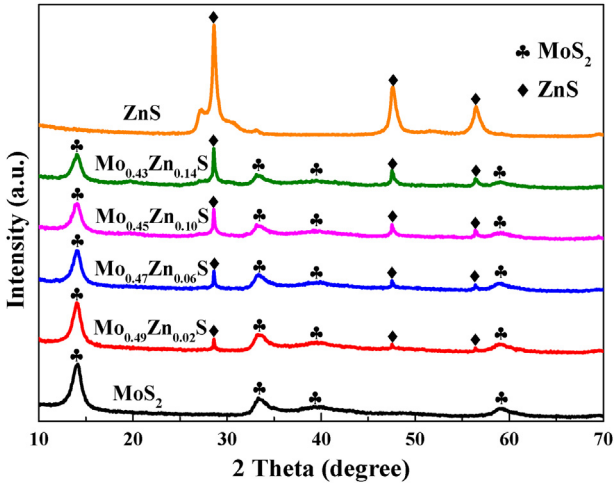

Fig. 1. XRD patterns of ZnS, MoS_2 and MoS_2/ZnS nano-heterojunction.

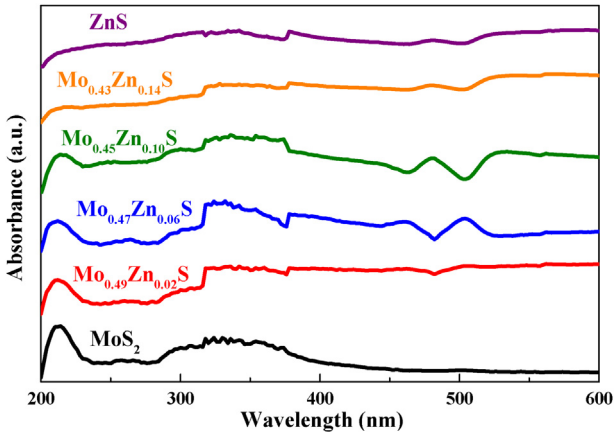

Fig. 2. UV–Vis absorbance spectra of ZnS, MoS_2 and MoS_2/ZnS nano-heterojunction.

MoS_2. MoS_2 had a wide adsorption in the visible light and ultraviolet (UV) region. The adsorption edge of ZnS sample was located around 370 nm wavelength, which was accordance with other works [39]. MoS_2 had a broader adsorption than ZnS in the visible light and ultraviolet (UV) region. MoS_2/ZnS nano-heterojunction except $Mo_{0.43}Zn_{0.14}S$ also possessed good adsorption in the visible light and ultraviolet (UV) region. Thus, MoS_2/ZnS nano-heterojunction was likely to be superior visible light and UV responsive photocatalysts for reduction of $[Au(S_2O_3)_2]^{3-}$.

The chemical compositions and elemental valence states of the products were investigated by XPS. XPS survey spectra clearly demonstrated the existence of Mo, S and Zn element in MoS_2/ZnS nano-heterojunctions (Fig. 3A). For pure MoS_2, the Mo $3d_{3/2}$ and $3d_{5/2}$ peaks were located at 232.68 and 229.48 eV (Fig. 3B), respectively, revealing the + 4 state of Mo in MoS_2 [40]. After coupling with ZnS, the Mo 3d peaks shifted to 231.88 ($3d_{3/2}$) and 228.98 eV ($3d_{5/2}$), respectively, which might be ascribed to the discontinuous growth of nanosheets due to the existence of Zn. Meanwhile, the peak at 234.78 eV (Mo^{VI}) probably originated from the interaction between ZnS and MoS_2. S 2p spectra (Fig. 3C) of the prepared samples were studied to further investigate the impact of ZnS on MoS_2. The peaks of $2p_{1/2}$ and $2p_{3/2}$ at 163.48 and 162.28 eV were consistent with the S^{2-} of MoS_2 [41]. The peaks observed at 162.73 and 161.18 eV could be assigned to ZnS [42]. After hybridization, S 2p peaks of MoS_2/ZnS nano-heterojunctions (162.98 eV, 161.78 eV) had a slight shift compared with MoS_2 and ZnS. In addition, the peaks of Zn $2p_{1/2}$ (1044.91 eV) and Zn $2p_{3/2}$

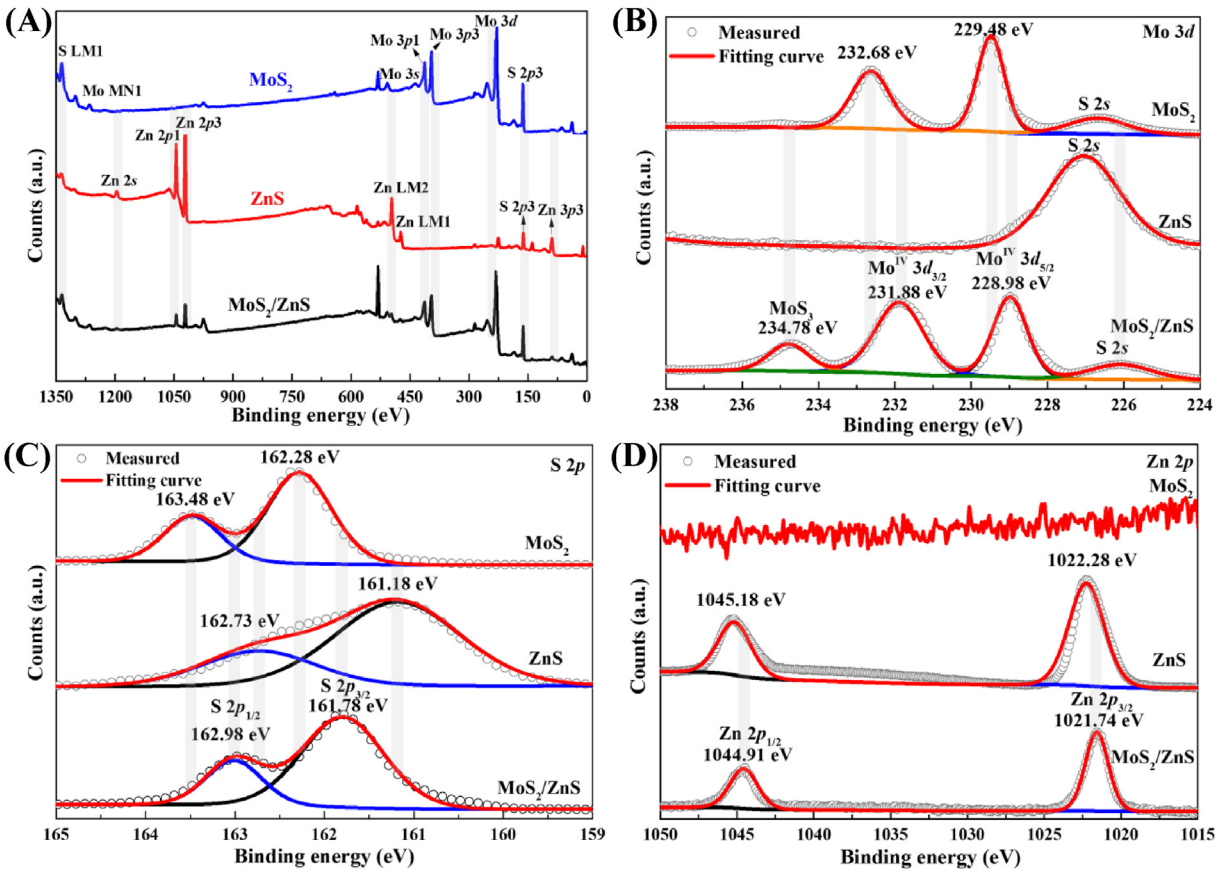

Fig. 3. XPS of ZnS, MoS_2 and MoS_2/ZnS nano-heterojunction: survey spectra (A), Mo 3d spectra (B), S 2p spectra (C) and Zn 2p spectra (D).

(1021.74 eV) of MoS_2/ZnS nano-heterojunction exhibited a shift in contrast to Zn 2p spectrum of ZnS (1045.18 eV, 1022.28 eV). These phenomena could be explained by partial electron transfers from ZnS to MoS_2, which further demonstrated the existence of strong electronic interactions between MoS_2 and ZnS, promoting the separation and transfer of photogenerated charges [23,43]. Therefore, the formation of heterojunction and Zn-S-Mo bonds would be very beneficial for the improvement of photocatalytic performances.

The morphologies and microstructures of ZnS, MoS_2 and MoS_2/ZnS nano-heterojunction were characterized by SEM and TEM (Figs. 4 and 5). From the SEM images (Fig. 4A1-A2), pure ZnS formed as spheres with plenty of small particles on the outer surface. The synthesized MoS_2 displayed as embroidered balls formed by countless ultrathin nanosheets, as exhibited in Fig. 4B1-B2. As for MoS_2/ZnS nano-heterojunction (Fig. 4C1-C2), it showed a similar morphology with MoS_2 but different density of ultrathin nanosheets. TEM and corresponding elemental mapping analysis were further provided for the investigation of Mo, Zn and S distribution (Fig. 5). Fig. 5A exhibited a similar result with SEM that the edges of MoS_2/ZnS nano-heterojunction were constituted by abundant of nanosheets. The high-resolution image clearly showed that MoS_2 with interlayer spacing of 0.651 nm [44,45] interlaced with ZnS with interlayer spacing of 0.313 nm [46] (Fig. 5B),

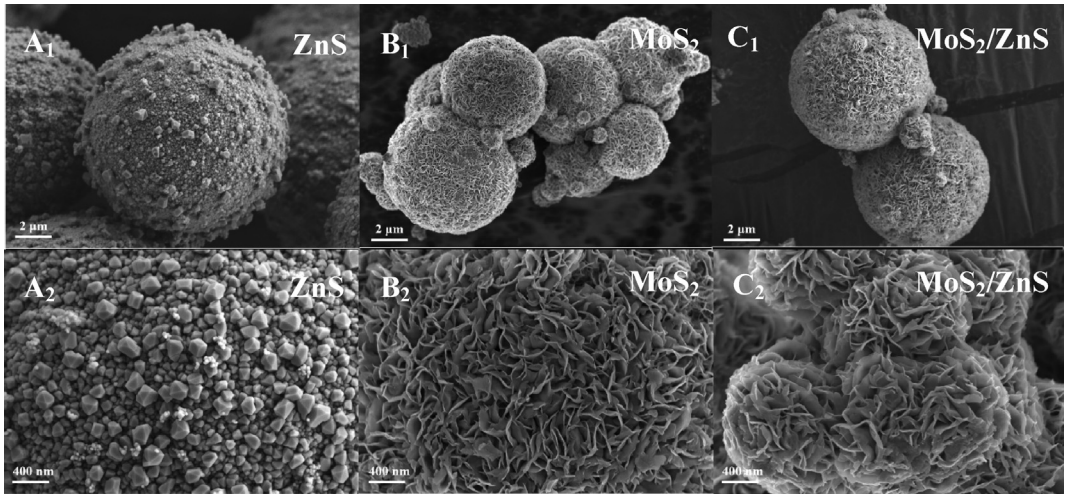

Fig. 4. SEM images of ZnS (A_1-A_2), MoS_2 (B_1-B_2) and MoS_2/ZnS nano-heterojunction (C_1-C_2) at different scales.

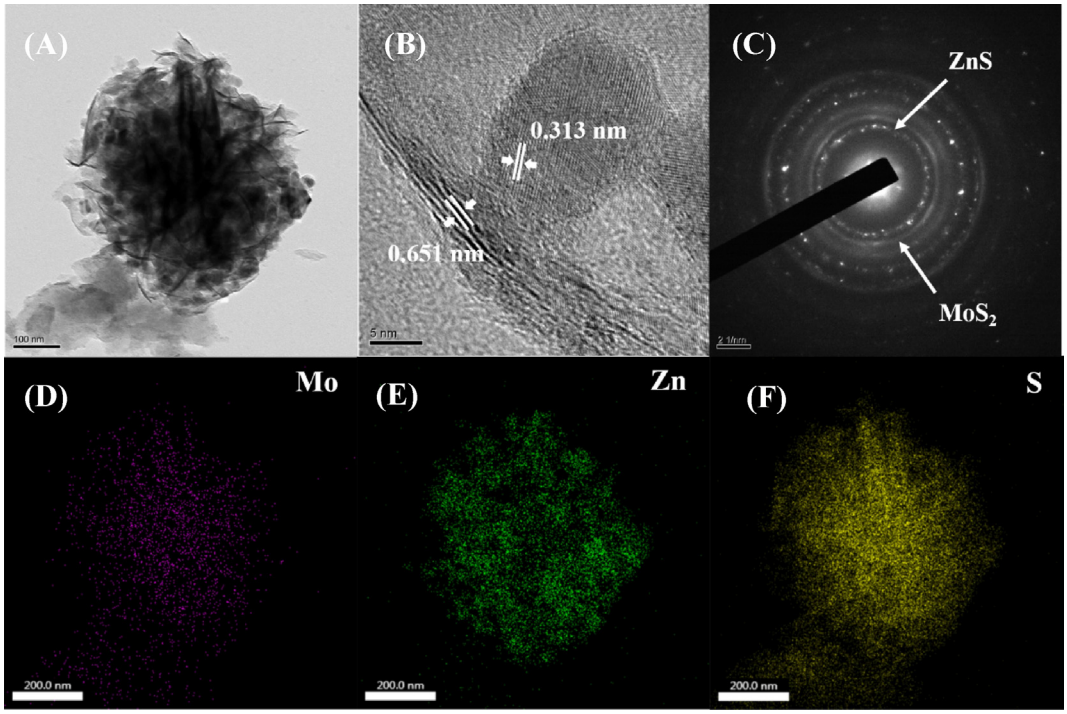

Fig. 5. TEM (A), HRTEM (B) and SAED (C) images of MoS_2/ZnS nano-heterojunction and corresponding EDS elemental mapping (D-F).

proving the existence of MoS_2 and ZnS. The selected area electron diffraction (SAED) pattern (Fig. 5C) indicated that the as-prepared sample consisted with polycrystal state of ZnS and hexagonal phase of MoS_2, which was consistent with the XRD results. The corresponding EDS elemental mappings revealed the uniform Mo distribution, concentrated Zn distribution and overlapped S distribution on Mo and Zn (Fig. 5D-F).

3.2. *In-situ reduction of $[Au(S_2O_3)_2]^{3-}$ on MoS_2/ZnS nano-heterojunction*

The photocatalytic reduction activities of $[Au(S_2O_3)_2]^{3-}$ on MoS_2/ZnS nano-heterojunction were tested under natural light irradiation. The photocatalytic performances of ZnS, MoS_2 and MoS_2/ZnS nano-heterojunction were exhibited in Fig. 6. It could be seen that the reduction capacity of $[Au(S_2O_3)_2]^{3-}$ on both ZnS and MoS_2 were lower than that on MoS_2/ZnS nano-heterojunction. For instance,

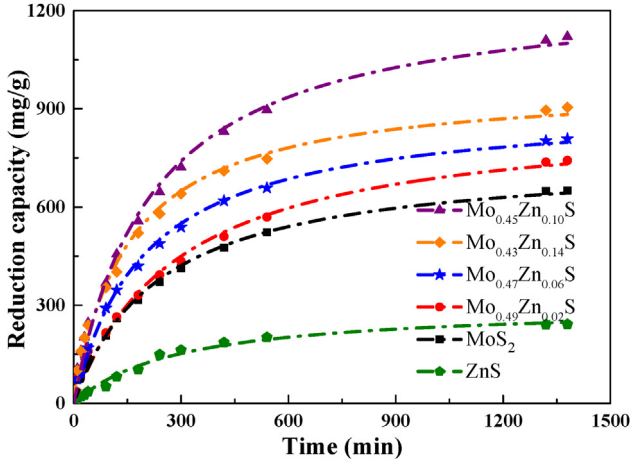

Fig. 6. Photocatalytic reduction performances of $[Au(S_2O_3)_2]^{3-}$ on ZnS, MoS_2 and MoS_2/ZnS nano-heterojunction as a function of time at pH of 10 and an initial $[Au(S_2O_3)_2]^{3-}$ concentration of 100 mg/L.

$Mo_{0.45}Zn_{0.10}S$ exhibited an extremely high reduction capacity of 1120.56 mg/g, which was 4.52 and 1.72 times of ZnS and MoS_2, respectively. The higher transferred efficiency and lower recombination of photogenerated electrons-holes pairs would account for the reduction capacity MoS_2/ZnS nano-heterojunction than that of ZnS and MoS_2. The reduction of $[Au(S_2O_3)_2]^{3-}$ on all the samples increased quickly as the increase of time and then reached balance. The balance might result from the saturation of the active sites of samples. Also, it was obvious that the reduction rate of $[Au(S_2O_3)_2]^{3-}$ on $Mo_{0.45}Zn_{0.10}S$ was the quickest among all the samples. Table 1 exhibited the comparison of the $[Au(S_2O_3)_2]^{3-}$ recovery capacity with same $[Au(S_2O_3)_2]^{3-}$ initial concentration by MoS_2/ZnS nano-heterojunction and other materials, which demonstrating the great recovery capacity of MoS_2/ZnS nano-heterojunction. The results demonstrated that MoS_2/ZnS nano-heterojunction had great potential in the recovery of gold from leach solution. In addition, it was found that the $[Au(S_2O_3)_2]^{3-}$ reduction capacity of MoS_2/ZnS nano-heterojunction increased with the Zn content and then decreased with further increase of Zn, which will be explained below.

Effect of pH on zata potential of $Mo_{0.45}Zn_{0.10}S$ and the reduction capacity of $[Au(S_2O_3)_2]^{3-}$ on $Mo_{0.45}Zn_{0.10}S$ were illustrated in Figs. 7 and 8, respectively. With the increase of pH, the negative potential increased quickly and then slowly, which demonstrated that the electrostatic interaction between H^+ and the negative charge of unsaturated S atoms in MoS_2 fast decreased and balanced. The reduction capacity increased quickly as increasing pH to 10 and then reached a plateau. As a result, the catalytic activity of MoS_2 principally originated from Mo edges as well as unsaturated S atoms. H^+ would compete with $[Au(S_2O_3)_2]^{3-}$ for the active sites, resulting in the decrease of $[Au(S_2O_3)_2]^{3-}$ reduction. Thus, $[Au(S_2O_3)_2]^{3-}$ reduction capacity increased as the decrease of H^+ (increase of pH). After pH higher than 10, very few H^+ presented in aqueous solution it is thereby unconspicuous effect on the reduction was observed. The reduction performances of $[Au(S_2O_3)_2]^{3-}$ on $Mo_{0.45}Zn_{0.10}S$ were investigated at various initial concentration. Fig. 9 illustrated that the reduction capacity increased with increasing the initial $[Au(S_2O_3)_2]^{3-}$ concentration.

$Mo_{0.45}Zn_{0.10}S$ was explored by XRD, XPS and TEM after being

Table 1
Comparison of the recovery capacity of MoS_2/ZnS nano-heterojunction and other materials.

Material	Recovery capacity (mg/g)	Recovery (%)	References
Cupric ferrocyanide-impregnated activated carbon	1.474	75	[14]
AgFC-impregnated activated carbon	1.212	70	[21]
MoS_2/ZnS	1120.56	91	This work

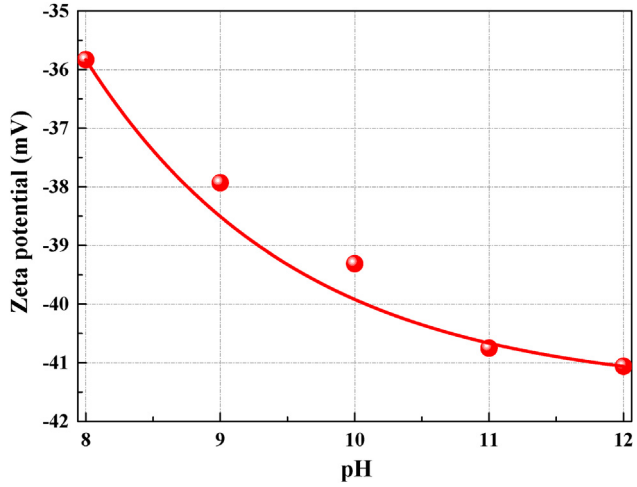

Fig. 7. Effect of pH on the zeta potential of $Mo_{0.45}Zn_{0.10}S$.

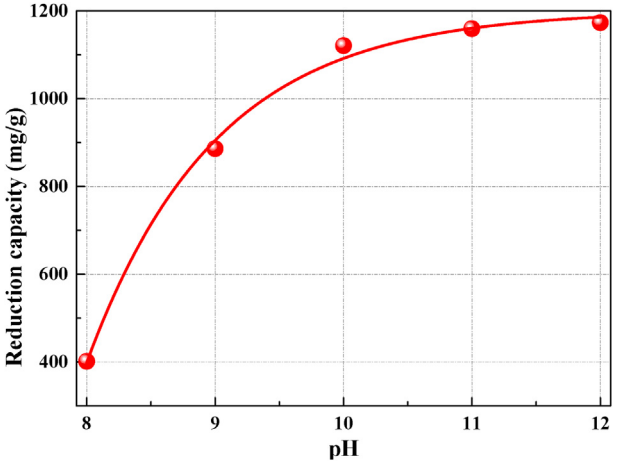

Fig. 8. Reduction capacity of $[Au(S_2O_3)_2]^{3-}$ on $Mo_{0.45}Zn_{0.10}S$ as a function of pH at an initial $[Au(S_2O_3)_2]^{3-}$ concentration of 100 mg/L.

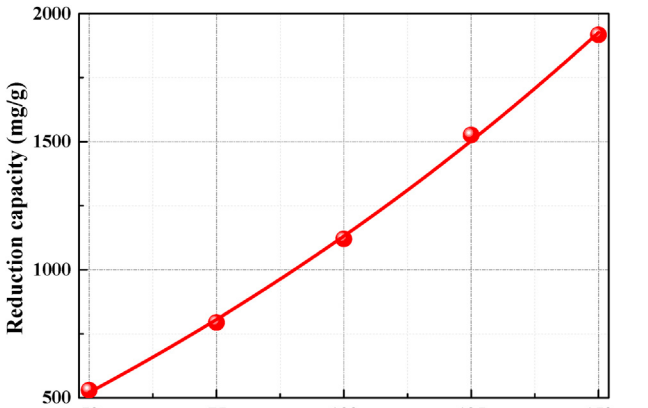

Fig. 9. Reduction capacity of $[Au(S_2O_3)_2]^{3-}$ on $Mo_{0.45}Zn_{0.10}S$ at various initial concentration and pH of 10.

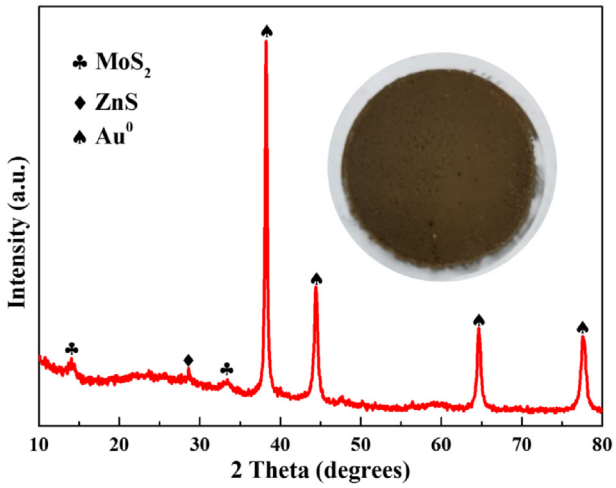

Fig. 10. XRD pattern of $Mo_{0.45}Zn_{0.10}S$ after $[Au(S_2O_3)_2]^{3-}$ reduction, and insert picture was digital picture of $Mo_{0.45}Zn_{0.10}S$ after $[Au(S_2O_3)_2]^{3-}$ reduction.

applied as catalyst in the $[Au(S_2O_3)_2]^{3-}$ aqueous solutions. Fig. 10 showed the XRD pattern and digital picture of $Mo_{0.45}Zn_{0.10}S$ after $[Au(S_2O_3)_2]^{3-}$ reduction. From the digital picture, it was worth noticing that a deposition layer with metal luster was formed on the surface of $Mo_{0.45}Zn_{0.10}S$, which could be identified to be Au^0. As for XRD pattern, the clear diffraction peaks at 38.3°, 44.4°, 64.7° and 77.6° were assigned to Au^0 [47], which well demonstrated that $[Au(S_2O_3)_2]^{3-}$ was in-situ reduced into Au^0 on $Mo_{0.45}Zn_{0.10}S$. Fig. 11A exhibited the wide-scan XPS spectra of $Mo_{0.45}Zn_{0.10}S$ after reduction of $[Au(S_2O_3)_2]^{3-}$ on it. Similar with XRD, high peaks of Au^0 were detected. The Mo 3d, S 2p and Zn 2p spectra shown in Fig. 11B, C and D revealed that no new peaks appeared and no changes occurred on Mo, S and Zn after being used for reducing $[Au(S_2O_3)_2]^{3-}$. Spectra of Au 4f was presented in Fig. 11E. Two peaks at 83.78 eV and 87.48 eV were Au^0 according to previous work [48]. The $[Au(S_2O_3)_2]^{3-}$ reduction on $Mo_{0.45}Zn_{0.10}S$ was further confirmed by the measurement of TEM-EDS. Fig. 12A–B displayed the morphological image of $Mo_{0.45}Zn_{0.10}S$ after $[Au(S_2O_3)_2]^{3-}$ reduction on it. Obviously, many nanoparticles with size of about 80–400 nm loaded on the thin sheets of $Mo_{0.45}Zn_{0.10}S$. Fig. 12C–F was the corresponding EDS elemental mapping of Mo, S, Zn and Au. It was clear that Mo distributed integrally on $Mo_{0.45}Zn_{0.10}S$, while Zn concentrated in part of $Mo_{0.45}Zn_{0.10}S$, and S overlapped with both Mo and Zn. The results well indicated that Zn presented in $Mo_{0.45}Zn_{0.10}S$ through heterojunction with MoS_2 in the form of ZnS. Interestingly, the distribution of Au was highly coincident with that of Zn, implying that $[Au(S_2O_3)_2]^{3-}$ preferred to be reduced into Au^0 at region where both Mo and Zn presented, further demonstrating that the MoS_2-ZnS heterojunction indeed enhanced the reduction of $[Au(S_2O_3)_2]^{3-}$.

3.3. Origin of the enhanced $[Au(S_2O_3)_2]^{3-}$ reduction on MoS_2/ZnS nano-heterojunction

The transient photocurrent response was displayed in Fig. 13 to

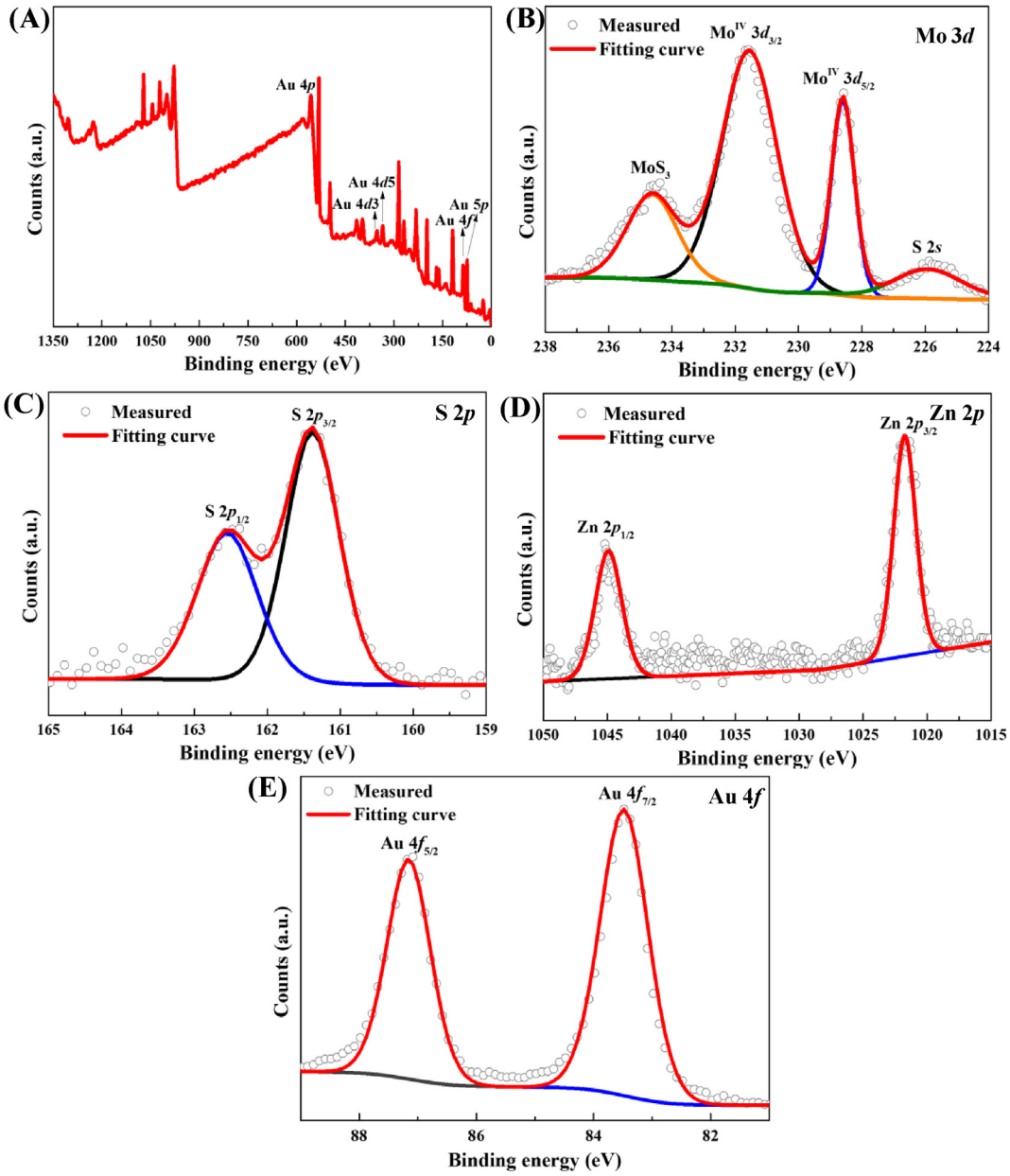

Fig. 11. XPS spectra of $Mo_{0.45}Zn_{0.10}S$ after $[Au(S_2O_3)_2]^{3-}$ reduction: wide-scan spectra (A), Mo 3d spectra (B), S 2p spectra (C), Zn 2p spectra (D) and Au 4f spectra (E).

investigate the separation efficiency of electrons and holes of ZnS, MoS_2 and MoS_2/ZnS nano-heterojunction. The nano-heterojunction enabled MoS_2/ZnS show higher photocurrent than ZnS and MoS_2, which can be ascribed to the fact that ZnS lowered the recombination rate of electrons and holes in MoS_2, indicating that MoS_2/ZnS nano-heterojunction had more photogenerated charges for the photocatalytic reduction. The photocurrent of MoS_2/ZnS nano-heterojunction first increased and then decreased with the increase of Zn. Meanwhile, $Mo_{0.45}Zn_{0.10}S$ possessed the highest photocurrent among all the prepared MoS_2/ZnS nano-heterojunction. The phenomenon was highly consistent with the $[Au(S_2O_3)_2]^{3-}$ reduction property of MoS_2/ZnS nano-heterojunction showing in Fig. 6. Therefore, it could be concluded that the photocatalytic performance of MoS_2/ZnS nano-heterojunction was attributed to the variation of photocurrent when MoS_2 and ZnS are coupled.

Fig. 14 displayed the EIS result for a further investigation on the photogenerated charges transfer and recombination of MoS_2/ZnS nano-heterojunction. The EIS Nyquist plots expressed that MoS_2/ZnS nano-heterojunction owed smaller semicircle than ZnS and MoS_2, revealing a faster photogenerated charges separation and transfer efficiency in MoS_2/ZnS nano-heterojunction. Similarly, $Mo_{0.45}Zn_{0.10}S$ possessed the fastest efficiency of photogenerated charges separation and transfer in all the MoS_2/ZnS nano-heterojunction samples.

To clarify the underlying mechanism of the enhanced photocatalytic activity, apparent quantum efficiencies (AQE) of MoS_2, ZnS and $Mo_{0.45}Zn_{0.10}S$ were calculated at $\lambda = 420$ nm. The catalytic mixture was irradiated under a 300 W Xe lamp for 5 h. The average incident irradiation of area was 3 cm^2. The reduced amount of $[Au(S_2O_3)_2]^{3-}$ in 5 h was mol for MoS_2, ZnS and $Mo_{0.45}Zn_{0.10}S$, respectively. All the calculations were given below.

$$AQE(\%) = \frac{(1 \times \textit{the number of } [Au(S_2O_3)_2]^{3-})}{\textit{the mumber of incident photons}} \times 100\% \quad (5)$$

As calculated, AQE of MoS_2, ZnS and $Mo_{0.45}Zn_{0.10}S$ was 0.38%, 0.14% and 0.73%, respectively. It was indicated that $Mo_{0.45}Zn_{0.10}S$ was highly-efficient photocatalyst for reducing $[Au(S_2O_3)_2]^{3-}$.

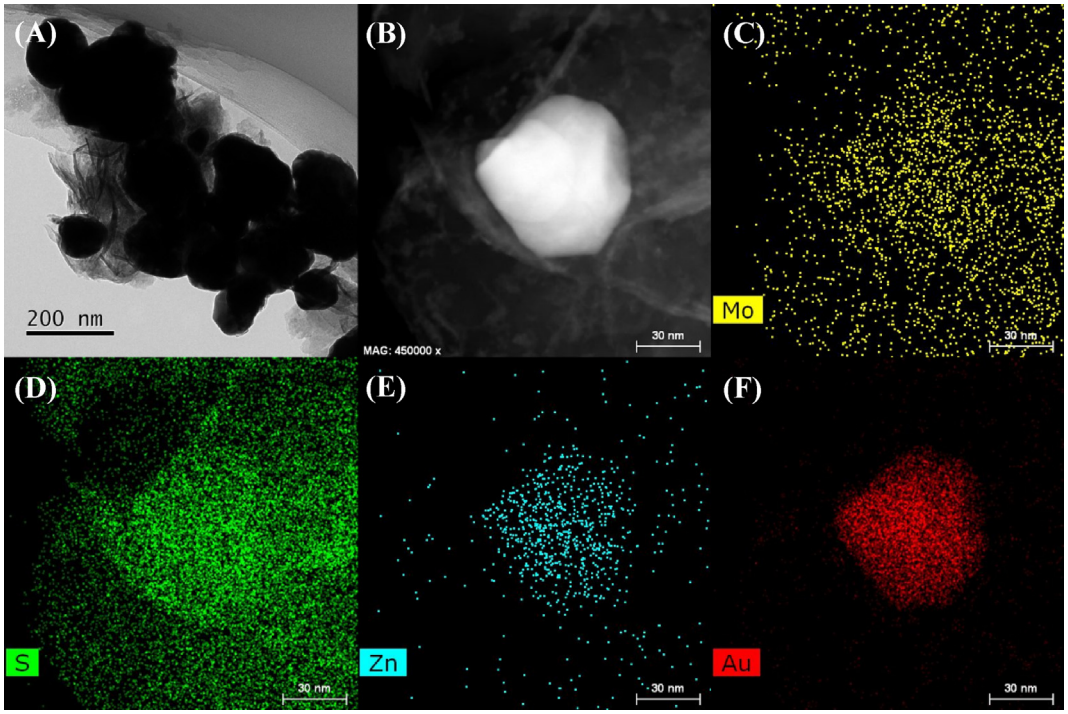

Fig. 12. TEM images of $Mo_{0.45}Zn_{0.10}S$ after $[Au(S_2O_3)_2]^{3-}$ reduction (A-B) and corresponding EDS elemental mapping (C-F).

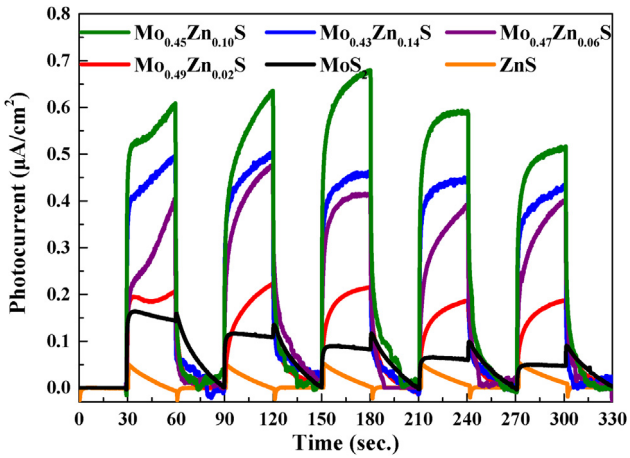

Fig. 13. Photocurrent responses of ZnS, MoS_2 and MoS_2/ZnS nano-heterojunction.

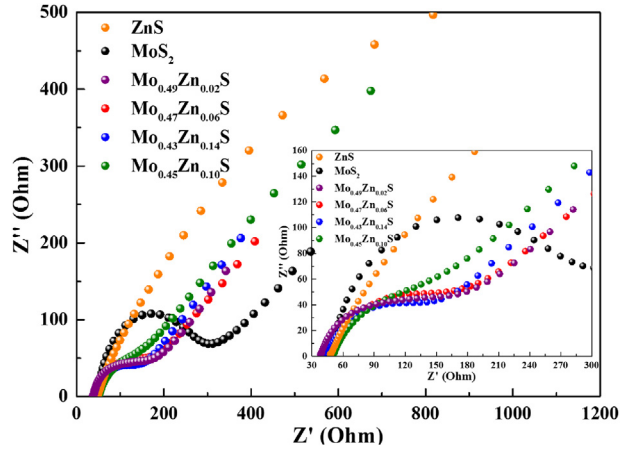

Fig. 14. EIS of ZnS, MoS_2 and MoS_2/ZnS nano-heterojunction.

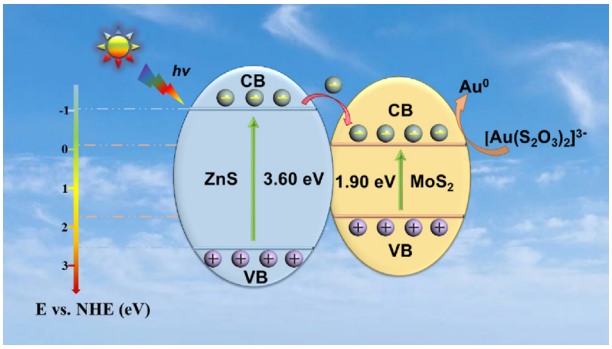

Fig. 15. Schematic illustration of photogenerated electrons transfer in MoS_2/ZnS nano-heterojunction and the photocatalytic reduction mechanism of $[Au(S_2O_3)_2]^{3-}$.

Based on the above results, the mechanism for highly effective reduction of $[Au(S_2O_3)_2]^{3-}$ by using MoS_2/ZnS nano-heterojunction as catalyst was proposed and schematically illustrated in Fig. 15. Figure showed the energy diagram indicating the formation of a Type I band heterostructure. The enhanced photocatalytic reduction of $[Au(S_2O_3)_2]^{3-}$ on $Mo_{0.45}Zn_{0.10}S$ was ascribed to the strong absorption of light, high transferred efficiency and low recombination of photogenerated electrons-holes pairs. Upon visible light irradiation, photogenerated electrons-holes pairs were produced in ZnS due to wider band gap than MoS_2. Then, the separated electrons were quickly transferred from ZnS to MoS_2 because of the lower conduction band (CB) positions.[23] Due to the strong interaction between gold and sulfur atoms, $[Au(S_2O_3)_2]^{3-}$ would be adsorbed on rich sulfur-containing $Mo_{0.45}Zn_{0.10}S$. The electrons on MoS_2 combined with $[Au(S_2O_3)_2]^{3-}$, leading to the in-situ reduction of $[Au(S_2O_3)_2]^{3-}$ into Au^0. In addition, large and intimate interfacial contact between ZnS and MoS_2 as exhibited in TEM results played an important role in benefiting the transfer of electrons and retardation of photogenerated charges recombination. According to previous work [49,50], $(S_2O_3)_2^{2-}$ could act as sacrificial agent consume the photogenerated holes. The possible chemical reactions of reducing $[Au(S_2O_3)_2]^{3-}$ using MoS_2/ZnS was

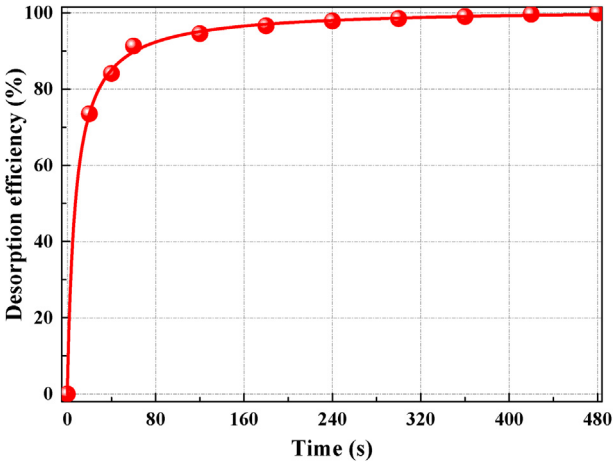

Fig. 16. The removal of Au^0 from $Mo_{0.45}Zn_{0.10}S$ in Na_2S solution.

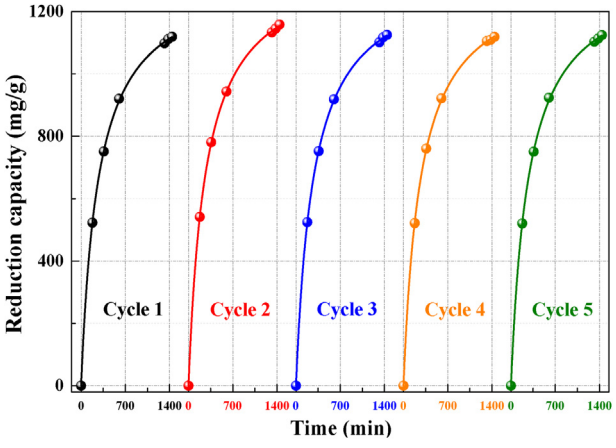

Fig. 17. Cycling tests of $[Au(S_2O_3)_2]^{3-}$ reduction on $Mo_{0.45}Zn_{0.10}S$ at pH of 10 and an initial $[Au(S_2O_3)_2]^{3-}$ concentration of 100 mg/L.

given in following equations.

$$MoS_2/ZnS \xrightarrow{hv} e^- + h^+ \quad (6)$$

$$2S_2O_3^{2-} + 2h^+ \rightarrow S_4O_6^{2-} \quad (7)$$

$$Au^+ + e^- \rightarrow Au^0 \quad (8)$$

Thus, MoS_2/ZnS nano-heterojunction would have great potential in gold leaching fields.

3.4. Recycle experiments of $[Au(S_2O_3)_2]^{3-}$ reduction on MoS_2/ZnS nano-heterojunction

Fig. 16 showed the removal of Au^0 from $Mo_{0.45}Zn_{0.10}S$ in Na_2S solution. It was obvious that the desorption of Au^0 from $Mo_{0.45}Zn_{0.10}S$ in Na_2S solution was relatively fast. A high desorption efficiency (91%) of Au could be reached in only 1 min and a complete desorption in less than 4 min. Five consecutive $[Au(S_2O_3)_2]^{3-}$ reduction reactions were performed to evaluate the stability of $Mo_{0.45}Zn_{0.10}S$ (Fig. 17). No obvious decrease of $[Au(S_2O_3)_2]^{3-}$ reduction capacity was observed, demonstrating the high stability of $Mo_{0.45}Zn_{0.10}S$.

4. Conclusions

Synthesized MoS_2/ZnS nano-heterojunction as a catalyst was proposed for efficient in-situ recovery of $[Au(S_2O_3)_2]^{3-}$ from leaching solution. $Mo_{0.45}Zn_{0.10}S$ exhibited remarkable high reduction capacity, which was higher than pure ZnS and MoS_2. The vast improvement originated from the strong absorption of light, high transferred efficiency and low recombination of photogenerated electrons-holes pairs and the strong interaction between gold and sulfur atoms. The desorption efficiency of Au^0 from MoS_2/ZnS nano-heterojunctions using Na_2S could realize a complete desorption in less than 4 min. MoS_2/ZnS nano-heterojunction had good cycling performances and stability. Therefore, MoS_2/ZnS nano-heterojunction was promising sustainable material for revering gold from leaching solutions owing to its high in-situ reduction capacity, excellent desorption efficiency and outstanding stability.

Declaration of Competing Interest

The authors declare that they have no known competing financial interests or personal relationships that could have appeared to influence the work reported in this paper.

Acknowledgements

The financial supports to this work from the National Natural Science Foundation of China (Nos. 51974216, 51704212 and 51704220), the Natural Science Foundation of Hubei Province (No. 2019CFB536) are gratefully acknowledged.

References

[1] E. Mohammadi, M. Pourabdoli, M. Ghobeiti-Hasab, A. Heidarpour, Ammoniacal thiosulfate leaching of refractory oxide gold ore, Int. J. Miner. Process. 164 (2017) 6–10, https://doi.org/10.1016/j.minpro.2017.05.003.
[2] M.G. Aylmore, W.P. Staunton, Effect of minerals on the stability of gold in copper ammoniacal thiosulfate solutions – The role of copper, silver and polythionates, Hydrometallurgy 143 (2014) 12–22, https://doi.org/10.1016/j.hydromet.2013.12.001.
[3] C. Wang, G. Lin, J. Zhao, S. Wang, L. Zhang, Y. Xi, X. Li, Y. Ying, Highly selective recovery of Au(III) from wastewater by thioctic acid modified Zr-MOF: Experiment and DFT calculation, Chem. Eng. J. 380 (2020) 122511, , https://doi.org/10.1016/j.cej.2019.122511.
[4] Z. Dong, J. Liu, W. Yuan, Y. Yi, L. Zhao, Recovery of Au(III) by radiation synthesized aminomethyl pyridine functionalized adsorbents based on cellulose, Chem. Eng. J. 283 (2016) 504–513, https://doi.org/10.1016/j.cej.2015.07.011.
[5] A. Sdiri, T. Higashi, R. Chaabouni, F. Jamoussi, Competitive removal of heavy metals from aqueous solutions by montmorillonitic and calcareous clays, Water. Air. Soil Pollut. 223 (2012) 1191–1204, https://doi.org/10.1007/s11270-011-0937-z.
[6] B. Fotoohi, L. Mercier, Some insights into the chemistry of gold adsorption by thiol and amine functionalized mesoporous silica in simulated thiosulfate system, Hydrometallurgy 156 (2015) 28–39, https://doi.org/10.1016/j.hydromet.2015.05.010.
[7] B. Feng, C. Yao, S. Chen, R. Luo, S. Liu, S. Tong, Highly efficient and selective recovery of Au(III) from a complex system by molybdenum disulfide nanoflakes, Chem. Eng. J. 350 (2018) 692–702, https://doi.org/10.1016/j.cej.2018.05.130.
[8] D.M. Muir, M.G. Aylmore, Thiosulphate as an alternative to cyanide for gold processing – issues and impediments, Miner. Process. Extr. Metall. 9553 (2017), https://doi.org/10.1179/0371955042250046.
[9] M. Karavasteva, Kinetics and deposit morphology of gold cemented on magnesium, aluminum, zinc, iron and copper from ammonium thiosulfate-ammonia solutions, Hydrometallurgy 104 (2010) 119–122, https://doi.org/10.1016/j.hydromet.2010.04.007.
[10] E. Guerra, D.B. Dreisinger, A study of the factors affecting copper cementation of gold from ammoniacal thiosulphate solution, Hydrometallurgy 51 (1999) 155–172.
[11] M.I. Jeffrey, D.M. Hewitt, X. Dai, S.D. Brunt, Ion exchange adsorption and elution for recovering gold thiosulfate from leach solutions, Hydrometallurgy 100 (2010) 136–143, https://doi.org/10.1016/j.hydromet.2009.11.003.
[12] M. Zhao, J. Zhao, Z. Huang, S. Wang, L. Zhang, One pot preparation of magnetic chitosan-cystamine composites for selective recovery of Au(III) from the aqueous solution, Int. J. Biol. Macromol. 137 (2019) 721–731, https://doi.org/10.1016/j.ijbiomac.2019.07.022.
[13] N.P. Gallagher, J.L. Hendrix, E.B. Milosavljevic, J.H. Nelson, L. Solujic, Affinity of activated carbon towards some gold(I) complexes, Hydrometallurgy 25 (1990) 305–316, https://doi.org/10.1016/0304-386X(90)90046-5.
[14] H. Yu, F. Zi, X. Hu, Y. Nie, P. Xiang, J. Xu, H. Chi, Adsorption of the gold-thiosulfate complex ion onto cupric ferrocyanide (CuFC)-impregnated activated carbon in aqueous solutions, Hydrometallurgy 154 (2015) 111–117, https://doi.org/10.1016/j.hydromet.2015.04.009.
[15] J. Kim, S. Byun, A.J. Smith, J. Yu, J. Huang, Enhanced electrocatalytic properties of transition-metal dichalcogenides sheets by spontaneous gold nanoparticle

decoration, J. Phys. Chem. Lett. 4 (2013) 1227–1232, https://doi.org/10.1021/jz400507t.
[16] Y. Li, H. Tian, C. Xiao, J. Ding, X. Chen, Efficient recovery of precious metal based on Au-S bond and electrostatic interaction, Green Chem. 16 (2014) 4875–4878, https://doi.org/10.1039/c4gc01375a.
[17] B. Yang, D. Wang, T. Wang, H. Zhang, F. Jia, S. Song, Effect of Cu^{2+} and Fe^{3+} on the depression of molybdenite in flotation, Miner. Eng. 130 (2019) 101–109, https://doi.org/10.1016/j.mineng.2018.10.012.
[18] X. Hong, J. Kim, S.F. Shi, Y. Zhang, C. Jin, Y. Sun, S. Tongay, J. Wu, Y. Zhang, F. Wang, Ultrafast charge transfer in atomically thin MoS_2/WS_2 heterostructures, Nat. Nanotechnol. 9 (2014) 682–686, https://doi.org/10.1038/nnano.2014.167.
[19] R.K. Chava, J.Y. Do, M. Kang, Enhanced photoexcited carrier separation in CdS-SnS_2 heteronanostructures: A new 1D–0D visible-light photocatalytic system for the hydrogen evolution reaction, J. Mater. Chem. A 7 (2019) 13614–13628, https://doi.org/10.1039/c9ta03059j.
[20] W. Fu, X. Guan, Z. Huang, M. Liu, L. Guo, Efficient photocatalytic overall water splitting over a core-shell GaInZnON@GaInON homojunction, Appl. Catal. B Environ. 255 (2019) 117741, , https://doi.org/10.1016/j.apcatb.2019.05.043.
[21] H. Yu, Adsorption of gold from thiosulfate solutions with chemically modified activated carbon, Adsorpt. Sci. Technol. 36 (2018) 408–428, https://doi.org/10.1016/j.ceramint.2017.08.021.
[22] F. Li, B. Dong, Construction of novel Z-scheme Cu2O/graphene/α-Fe_2O_3 nanotube arrays composite for enhanced photocatalytic activity, Ceram. Int. 43 (2017) 16007–16012, https://doi.org/10.1016/j.ceramint.2017.08.021.
[23] S. Zhang, H. Yang, H. Gao, R. Cao, J. Huang, X. Xu, One-pot synthesis of CdS irregular nanospheres hybridized with oxygen-incorporated defect-rich MoS_2 ultrathin nanosheets for efficient photocatalytic hydrogen evolution, ACS Appl. Mater. Interfaces 9 (2017) 23635–23646, https://doi.org/10.1021/acsami.7b03673.
[24] M.E. Aguirre, R. Zhou, A.J. Eugene, M.I. Guzman, M.A. Grela, Cu_2O/TiO_2 heterostructures for CO_2 reduction through a direct Z-scheme: protecting Cu_2O from photocorrosion, Appl. Catal. B Environ. 217 (2017) 485–493, https://doi.org/10.1016/j.apcatb.2017.05.058.
[25] K.S. Ranjith, R.B. Castillo, M. Sillanpaa, R.T. Rajendra Kumar, Effective shell wall thickness of vertically aligned ZnO-ZnS core-shell nanorod arrays on visible photocatalytic and photo sensing properties, Appl. Catal. B Environ. 237 (2018) 128–139, https://doi.org/10.1016/j.apcatb.2018.03.099.
[26] S. Ahluwalia, N.T. Prakash, R. Prakash, B. Pal, Improved degradation of methyl orange dye using bio-co-catalyst Se nanoparticles impregnated ZnS photocatalyst under UV irradiation, Chem. Eng. J. 306 (2016) 1041–1048, https://doi.org/10.1016/j.cej.2016.08.028.
[27] S.N. Azizi, P. Shakeri, M.J. Chaichi, A. Bekhradnia, M. Taghavi, M. Ghaemy, The use of imidazolium ionic liquid/copper complex as novel and green catalyst for chemiluminescent detection of folic acid by Mn-doped ZnS nanocrystals, Spectrochim. Acta – Part A Mol. Biomol. Spectrosc. 122 (2014) 482–488, https://doi.org/10.1016/j.saa.2013.11.036.
[28] C.M. Wu, C.I. Lin, Y.C. Peng, The effects of catalysts on the carbothermic reduction of zinc sulfide in the presence of calcium oxide, J. Chinese Inst. Chem. Eng. 38 (2007) 91–93, https://doi.org/10.1016/j.jcice.2006.12.002.
[29] J. Hu, G. Wang, C. Guo, D. Li, L. Zhang, J. Zhao, Au-catalyst growth and photoluminescence of zinc-blende and wurtzite ZnS nanobelts via chemical vapor deposition, J. Lumin. 122–123 (2007) 172–175, https://doi.org/10.1016/j.jlumin.2006.01.074.
[30] S.Y. Cheon, J.S. Yoon, K.H. Oh, K.Y. Jang, J.H. Seo, J.Y. Park, S. Il Choi, W.S. Seo, G. Lee, K.M. Nam, Sonochemical synthesis of ZnO-ZnS core-shell nanorods for enhanced photoelectrochemical water oxidation, J. Am. Ceram. Soc. 100 (2017) 3825–3834, https://doi.org/10.1111/jace.14935.
[31] G. Panthi, N.A.M. Barakat, M. Park, H.Y. Kim, S.J. Park, Fabrication of PdS/ZnS NPs doped PVAc hybrid electrospun nanofibers: effective and reusable catalyst for dye photodegradation, J. Ind. Eng. Chem. 21 (2015) 298–302, https://doi.org/10.1016/j.jiec.2014.02.036.
[32] G. Naresh, P.L. Hsieh, V. Meena, S.K. Lee, Y.H. Chiu, M. Madasu, A.T. Lee, H.Y. Tsai, T.H. Lai, Y.J. Hsu, Y.C. Lo, M.H. Huang, Facet-dependent photocatalytic behaviors of ZnS-decorated Cu_2O polyhedra arising from tunable interfacial band alignment, ACS Appl. Mater. Interfaces. 11 (2019) 3582–3589, https://doi.org/10.1021/acsami.8b19197.
[33] X. Wang, W.C. Peng, X.Y. Li, Photocatalytic hydrogen generation with simultaneous organic degradation by composite CdS-ZnS nanoparticles under visible light, Int. J. Hydrogen Energy 39 (2014) 13454–13461, https://doi.org/10.1016/j.ijhydene.2014.04.034.
[34] S.V. Tambwekar, M. Subrahmanyam, Enhanced photocatalytic H_2 production over CdS-ZnS supported on super basic oxides, Int. J. Hydrogen Energy 23 (1998) 741–744, https://doi.org/10.1016/s0360-3199(97)00126-2.
[35] I. Tsuji, A. Kudo, H2 evolution from aqueous sulfite under visible-light irradiation over Pb and halogen-codoped ZnS photocatalysts, J. Photochem. Photobiol. A Chem. 156 (2003) 249–252, https://doi.org/10.1016/S1010-6030(02)00433-1.
[36] C. Liu, F. Jia, Q. Wang, B. Yang, S. Song, Two-dimensional molybdenum disulfide as adsorbent for high-efficient Pb(II) removal from water, (2017) 220–228.
[37] K. Sun, F. Jia, B. Yang, C. Lin, X. Li, S. Song, Synergistic effect in the reduction of Cr (VI) with Ag-MoS_2 as photocatalyst, Appl. Mater. Today 2 (2019) 100453, , https://doi.org/10.1016/j.apmt.2019.100453.
[38] B. Zhu, B. Lin, Y. Zhou, P. Sun, Q. Yao, Y. Chen, B. Gao, Enhanced photocatalytic H2 evolution on ZnS loaded with graphene and MoS_2 nanosheets as cocatalysts, J. Mater. Chem. A 2 (2014) 3819–3827, https://doi.org/10.1039/c3ta14819j.
[39] M. Joy, A.P. Mohamed, K.G.K. Warrier, U.S. Hareesh, Visible-light-driven photocatalytic properties of binary MoS_2/ZnS heterostructured nanojunctions synthesized via one-step hydrothermal route, New J. Chem. 41 (2017) 3432–3442, https://doi.org/10.1039/c6nj03727e.
[40] X. Zhang, F. Jia, B. Yang, S. Song, Oxidation of molybdenum disulfide sheet in water under in situ atomic force microscopy observation, J. Phys. Chem. C 121 (2017) 9938–9943, https://doi.org/10.1021/acs.jpcc.7b01863.
[41] T. Sun, Z. Li, X. Liu, L. Ma, J. Wang, Oxygen-incorporated MoS_2 microspheres with tunable interiors as novel electrode materials for supercapacitors, J. Power Sources 352 (2017) 135–142, https://doi.org/10.1016/j.jpowsour.2017.03.123.
[42] N.L. Reddy, V.N. Rao, M.M. Kumari, M. Sathish, S., Muthukonda Venkatakrishnan, Development of high quantum efficiency CdS/ZnS core/shell structured photocatalyst for the enhanced solar hydrogen evolution, Int. J. Hydrogen Energy 43 (2018) 22315–22328, https://doi.org/10.1016/j.ijhydene.2018.10.054.
[43] Y. Zhao, W. Wang, M. Chen, R. Wang, Z. Fang, The synthesis of ZnS@MoS_2 hollow polyhedrons for enhanced lithium storage performance, CrystEngComm 20 (2018) 7266–7274, https://doi.org/10.1039/c8ce01306c.
[44] H. Zhang, X. Lv, F. Wang, Z. Hu, H. Han, X. Fan, J. Ji, Vertically aligned, polypyrrole encapsulated MoS2 / graphene composites for high-rate LIBs anode, Ceram. Int. 44 (2018) 7611–7617, https://doi.org/10.1016/j.ceramint.2018.01.180.
[45] W. Zhan, F. Jia, Y. Yuan, C. Liu, K. Sun, B. Yang, Controllable incorporation of oxygen in MoS2 for efficient adsorption of Hg^{2+} in aqueous solutions, J. Hazard. Mater. 384 (2020) 1–10, https://doi.org/10.1016/j.jhazmat.2019.121382.
[46] J. Feng, J. Liu, X. Cheng, J. Liu, M. Xu, J. Zhang, Hydrothermal cation exchange enabled gradual evolution of Au@ZnS–AgAuS yolk-shell nanocrystals and their visible light photocatalytic applications, Adv. Sci. 5 (2018) 1–7, https://doi.org/10.1002/advs.201700376.
[47] Y. Yuan, B. Yang, F. Jia, S. Song, Reduction mechanism of Au metal ions into Au nanoparticles on molybdenum disulfide, Nanoscale 11 (2019) 9488–9497, https://doi.org/10.1039/c8nr09420a.
[48] Y. Shi, J.K. Huang, L. Jin, Y. Te Hsu, S.F. Yu, L.J. Li, H.Y. Yang, Selective decoration of Au nanoparticles on monolayer MoS_2 single crystals, Sci. Rep. 3 (2013) 1–7, https://doi.org/10.1038/srep01839.
[49] S. Gámez, K. Garcés, E. de la Torre, A. Guevara, Precious metals recovery from waste printed circuit boards using thiosulfate leaching and ion exchange resin, Hydrometallurgy 186 (2019) 1–11, https://doi.org/10.1016/j.hydromet.2019.03.004.
[50] O. Sitando, G. Senanayake, X. Dai, A.N. Nikoloski, P. Breuer, A review of factors affecting gold leaching in non-ammoniacal thiosulfate solutions including degradation and in-situ generation of thiosulfate, Hydrometallurgy 178 (2018) 151–175, https://doi.org/10.1016/j.hydromet.2018.02.016.